Computers and Structures 305 (2024) 107535

Contents lists available at ScienceDirect

Computers and Structures

journal homepage: www.elsevier.com/locate/compstruc

Three-dimensional meso-scale modeling of asphalt concrete

G. Mazzucco *, B. Pomaro, V.A. Salomoni, C.E. Majorana

Department of Civil, Environmental and Architectural Engineering, University of Padova, Via F. Marzolo 9, 35131 Padova, Italy

ARTICLE INFO

Keywords:
Creep
Elasto-plasticity
Visco-elasto-plasticity
Concrete asphalt
Binder
Bituminous materials
Meso-scale

ABSTRACT

An efficient method to address the three-dimensional modeling of the visco-elasto-plastic material behavior, specifically of bituminous conglomerates used in asphalt concrete production, is proposed. The method resorts to one of the most recent formulations for asphalt creep modeling, represented by the modified Huet-Sayegh fractional rheological model. The Grünwald-Letnikov representation of the fractional operator is adopted to treat the operator numerically in an efficient manner. Further, a coupling scheme between the creep model and elasto-plasticity is proposed by adopting the additive decomposition of the total strain tensor. This enables the numerical assessment of the mechanical behavior for bituminous materials under short- to long-term loading. In this context, both constant strain rate tests, and creep recovery tests are numerically simulated.
Numerical analyses are conducted at the meso-scale with the aim to evaluate the development of inelastic strains in the binder during creep, due to the local interaction between the different material components.

1. Introduction

With the recent increase in computational power, the adoption and applicability of complex material models and complex geometries are becoming practicable. In this context, the evolution of numerical constitutive models to simulate the mechanical behavior of building materials has reached today a remarkable level of development.
Materials such as cement concrete, or asphalt concrete are very heterogeneous media. They are, generally, studied at the homogeneous macro-scale, when the assessment of their mechanical behavior is needed at the structural level. However, if local effects are to be accounted for, a meso-mechanics approach is nowadays desirable and feasible. At a meso-scale level the heterogeneous nature of the material is explicitly modeled through its material constituents. Further, each phase is characterized by differentiated material properties and even different mechanical behaviors. Thus, it is expected that the interactions between the constituents determine the bulk-scale response.
The attractiveness of a meso-scale approach is mainly related to the possibility to investigate the development of local stresses and strains in the different material components. This is expected to provide useful insight into damage initiation and propagation, thus ultimately determining the material performance at the macro-scale. In this manner, design and control issues like mixture optimization, sampling, or, in the case of asphalt concrete, the contrast to raveling and rutting, can be more efficiently addressed at the scale of the constituents.

The application to meso-mechanics for bituminous conglomerates dates back to the work by Rothenburg et al. [1]. Since then, various upgrades on this field have been made. Limited to the continuous modeling approach, primarily represented by the Finite Element Method (FEM), remarkable advancements are found in [2–6]. The effort in research has been twofold. On one side it has focused towards the development of appropriate constitutive response models that can capture the nonlinearities and the long-term effects typically associated to binder materials for asphalt concrete production, for a wide range of loading magnitudes and rates; on the other side, to the development of adequate geometry reconstruction techniques for solid-modeling related issues.
As regards the former aspect, various constitutive models have been developed to describe the visco-elastic behavior of asphalt materials. Specifically, a variety of one-dimensional rheological models exists in the literature describing the time and temperature dependence of the mechanical behavior of bituminous materials in the visco-elastic regime. The most frequently adopted mechanical models include some combinations of linear spring and linear dashpot elements [7], leading to the generalized Voigt-Kelvin model (also in the form of the Burgers' model), and the generalized Maxwell model. More recently, from the pioneering works by Gemant [8] and Bagley and Torvik [9] it was observed that the non-local nature of creep can be efficiently described by the fractional derivative operator [10–14]. Thus, visco-elastic models based on fractional calculus are emerging as an alternative approach to more consolidated ones. They incorporate fractional derivative terms, also called

* Corresponding author.
E-mail address: gianluca.mazzucco@unipd.it (G. Mazzucco).

https://doi.org/10.1016/j.compstruc.2024.107535
Received 2 November 2023; Accepted 3 September 2024
Available online 19 September 2024

parabolic dashpot elements, or springpots, into the constitutive models to capture the typical non-local, memory-dependent behavior of the binder.

Research on the field of the visco-elasto-plastic modeling of bituminous materials or asphalt conglomerates, more generally, is more limited. Schwartz et al. [15] and Underwood and Kim [16] have developed a one-dimensional model based on the Schapery continuum damage formulation [17]. A one-dimensional visco-elasto-plastic model combining a generalized Maxwell model and a hardening visco-plastic element has been proposed by Giunta and Pisano [18]. Darabi et al. [19] are the authors of a thermo-visco-elasto-damage model for asphalt concrete coupling Schapery's nonlinear visco-elasticity [20], Perzyna-type visco-plasticity [21] with a generalized Drucker–Prager-type yield surface [22], and Kachanov [23]'s damage theory. The model has been used to conduct three-dimensional meso-mechanical studies in [24]. Pasetto and Baldo [25] have formulated a three-dimensional visco-elasto-plastic model in the framework of associative plasticity and isotropic hardening, for the irreversible plastic strains, and thermodynamically consistent.

Fractional models for visco-elasticity and visco-elasto-plasticity have been proposed in [26–29] in a one-dimensional form. A 3D extension of a fractional visco-elastic model for bitouminous materials has been developed in [30] to simulate the mechanical behavior of mesoscopic, idealized in geometry, porous asphalt mixtures.

In relation to the aspect related to the geometrical reconstruction of asphalt at the scale of its constituents, the meso-mechanics approach encompasses the definition of a Representative Elementary Volume (REV). It represents also a control volume for the random distribution of inclusions of various shape and size. This challenging task has been more and more assisted by imaging processing technologies, able to capture the real asphalt concrete mixture geometry [31–39]. However, techniques such as 3D laser scanner or industrial computed tomography have a limit in the number of samples that they can treat, so restricting the number of corresponding models than can be generated out of the scanned images. More versatile tools are represented by random aggregate distribution algorithms. This method allows the reconstruction of an unlimited number of realizations of inclusions within a control volume, based on minimum distance procedures. This is achieved by generating and randomly packing aggregates avoiding overlapping.

Aggregates can assume, in the simplest case, ideal shapes, like spheres or ellipsoids [40–44], or more realistic irregular polyedral shapes [45–49]. A common challenge to most existing random distribution algorithms is the difficulty to meet an optimum aggregate packing density, or to reach the prescribed aggregate volume ratio as it is found in the real specimens. Thus, an effort has been made by more recent studies towards the development of approaches that can randomly pack inclusions in compliance with predefined grading curves [50–52].

This work aims to address both aspects involving asphalt concrete modeling, the rheological and the geometrical one, in a novel manner. To the authors' best knowledge, no prior studies have utilized a fractional visco-elastic model in conjunction with plasticity to predict the three-dimensional mechanical behavior of asphalt concrete, incorporating a realistic 3D representation of the material's mesostructure.

The fractional formulation for visco-elasticity has been recently introduced in the literature, but more on a one-dimensional space. When a 3D extension of a fractional model is considered, numerical analyses are conducted on a simplified idealized geometry, or inelastic effects due to plasticity are not taken into account in the constitutive model. Building on this perspective, the present work aims to develop a more comprehensive approach to asphalt material modeling. This approach seeks to be complete both in terms of the constitutive modeling of the material and the accurate representation of its complex geometry, characteristic of a multi-phase composite geomaterial.

With this objective in mind, the present study introduces a numerical coupling scheme between creep and elasto-plasticity within a three-dimensional formulation. Long-term effects are accounted for utilizing a fractional model for visco-elasticity. This approach is specifically selected for its requisite capability to explain laboratory measured response data at a reasonable computational cost. Differently, inelastic plastic effects are determined within the framework of associative plasticity. Further, realistic inclusions in the conglomerate are reconstructed using Bézier's polynomial approximation of ideal ellipsoid surfaces. Their random location within the control volume and the random spacing between particles are consistent with a given grading curve and degree of asphalt macro-porosity, achieved through a specific numerical tool developed in this study.

2. Meso-scale reconstruction

Realistic meso-scale geometries for composite samples can be obtained in different manners. Two main techniques are, generally, worth mentioning: the reconstruction via X-ray computed tomography (CT) results, and the simulation via random distribution algorithms. The first method is to be adopted when the real shape and distribution of inclusions inside the sample are pursued. For this reason, a real sample must be available and scanned by means of a CT machine. The second method, here selected, is an attractive alternative when many sample realizations, equally possible, are needed of a REV of a composite material, with given grading curve and aggregate volume fraction.

In this Section a procedure to numerically reconstruct a realistic meso-scale solid model is discussed. It consists in the following main steps:

- Development of a random distribution algorithm for the inclusions, in agreement with a given grading curve and a given aggregate volume fraction;
- Reconstruction of the inclusion shape;
- Reconstruction of the surrounding matrix phase.

2.1. Random distribution algorithm for solid inclusions

It is assumed that the inclusions are roundish. Thus, they can ideally be approximated by means of circumscribed ellipsoid shapes of different dimensions, in agreement with the material grading curve. At each iteration a new ellipsoid inclusion is added into the virtual sample, typically represented by the cubic or cylindrical real volume of the specimen. This control volume bounds the space where a new aggregate can be located. On the control volume a check is performed of non-overlapping between each new inclusion with the previous ones. A complete description of this technique can be found in [50]. The current study adopts this methodology, enhancing it by incorporating a compaction algorithm designed to simulate aggregate sedimentation during the mixing process under the influence of gravity. This enhancement to the method previously developed by the same authors is illustrated in Fig. 1, presented here in a simplified 2D format. During the iterative procedure in which a new ellipsoid inclusion is added within the control volume, the compaction algorithm is activated every m new added inclusions (see Fig. 1 a)). First, the existing inclusions are ordered from the lower to the upper along the coordinate direction of the gravity acceleration vector (Fig. 1 b)); next, each inclusion is projected along this direction, and the maximum distance between inclusions, to avoid overlapping in case of their translation along the same direction, is evaluated (Fig. 1 c)); finally, aggregates motion along the gravity direction is accomplished, based on the previously computed maximum distances.

An example of the performance of the proposed random aggregate algorithm, inclusive of this improved compaction technique, is reported in Fig. 2 a).

For this specific example, the reference grading curve of a cylindrical sample provided in [53] is used as a comparison for the numerical simulation. A cut-off nominal diameter equal to 4 mm has been necessarily assumed in order to limit the grain size of the solid model to the explicit representation of aggregates with nominal diameter equal or greater to the chosen cut-off size. This leads to a specific target ratio

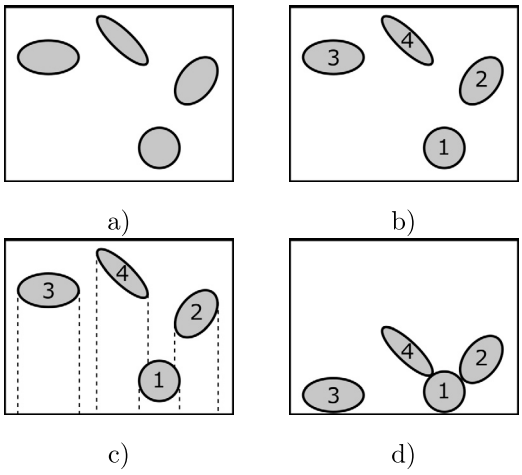

Fig. 1. Compaction procedure in 2D space. Initial sequence, after adding $m = 4$ inclusions a); numbering of inclusions from the lower to the upper b); aggregates projection along the direction of the gravity acceleration vector c); performed compaction d).

between the coarse aggregate volume fraction and the sample volume, which corresponds to $a/s = 0.65$ for the specific benchmark test. A realization of the distribution of spherical particles obtained by using the proposed technique is reported in Fig. 2 b), with the corresponding comparison between the real and the simulated grading curve characterizing the sample.

2.2. Reconstruction of the inclusion shape

Normally, real inclusions are roundish, if not edgy polyhedral, because they come from crushed stone or gravel. Thus, the shape of real aggregates can be very complex. If roundish, however, the ellipsoid model can be adopted in good approximation as a reference circumscribed regular volume, as depicted in Fig. 3. To produce realistic roundish solid shapes of the conglomerate inclusions, a modification of the ideal ellipsoid geometry is obtained by using the Bézier's polynomial formulation. The Bézier curve is a parametric spline that finds broad application in computer graphics. It allows to represent a very complex geometry starting from two anchor points, and some control points. The generalized primitive Bézier function of order n can be construed starting from Bernstein basis polynomials as

$$\mathbf{b} = \sum_{i=0}^{n} \frac{n!}{i!(n-i)i} t^i (1-t)^{n-i} \mathbf{x}_i \tag{1}$$

where $\mathbf{x}_0$ and $\mathbf{x}_n$ are the coordinates of the anchor points with respect to a global reference system; $\mathbf{x}_i$ (with $i \neq 0, n$) are those of the control points, and $0 \leq t \leq 1$ is the percentage progress of the curve.
A Bézier -type approximation of a 2D section profile of a real aggregate shape is reported in Fig. 4, as an example. The red solid line is the polynomial; the magenta markers are the anchor points, and the yellow ones are the control points. It is noted with this example that the Bézier polynomials are able to satisfactorily reproduce a complex geometry with a limited number of control points.
Without lack in generality, the same concept can be extended to the 3D space. To obtain realistic aggregate volumes, several anchor points, randomly distributed over the ideal ellipsoid surface, are defined. Further, the control points are chosen, again, randomly among the points external to the ellipsoid surface.

Nevertheless, Fig. 5 shows that not all the random configurations for the control points are admissible. Indeed, the external ellipsoidal surface constitutes a constraint to the polynomials. The proposed procedure has been implemented with a script programmed in Python language, able to generate an .STL file containing information on the final inclusion shapes.

In Fig. 6 a) various examples of different solid geometries, generated by applying the Bézier approximation to four ideal ellipsoid surfaces of different dimensions and orientations, are presented. Fig. 6 b) reports a complete reconstruction of a random aggregate distribution compliant with a prescribed grading curve, for a cylindrical sample of diameter $d = 100$ mm and height $h = 30$ mm. It is a result of the adoption of the random numerical tool illustrated in the previous sub-section 2.1, and the outer surface modification procedure proposed in the present sub-section.

2.3. Reconstruction of the surrounding matrix phase

In the case of a cementitious material, a "matrix" includes the binder material and the finer aggregate fraction, which is not explicitly represented as "aggregate" for computational reasons. In concrete asphalt materials the binder can be regarded as a thin layer surrounding the aggregates, and adhering to their outer surface, having viscous properties. From the solid modeling viewpoint, the sketch on how to generate the matrix volume is shown in Fig. 7 in a 2D space and for circular inclusions, for sake of simplicity.

After applying the random aggregate distribution procedure and the outer surfaces distortion, all the inclusions are located into the three-dimensional control volume (Fig. 7 a). Next, starting from the center of each inclusion, an offset of its outer surface is performed, in order to reconstruct for each inclusion a twin external surface at a desired thickness from the original one. The thickness value is assigned in relation to the average binder thickness surrounding aggregates in a real sample (Fig. 7 b). In order to remove all the overlapping parts of surfaces and volumes associated to the twin geometry, boolean operations are conducted in a CAD environment (Fig. 7 c). Finally, the resulting outer surfaces are smoothed to remove any unrealistic sharp edge, as depicted in Fig. 7 d). This last procedure is crucial, in order to meet the target degree of macroporosity that generally characterizes concrete asphalt. This is obtained by varying the smoothing parameters accordingly, at the point that macroporosity between inclusions can be present or not (see Fig. 8). If present, it can reach any desired degree by simply adjusting the smoothing parameters. In this context, Fig. 9 shows simulated concrete asphalt samples of different degrees of macroporosity, obtained by using the proposed technique, and, more specifically, different smoothing parameters for the last operation. It is underlined that the boolean operation between surfaces and volumes, together with the surface smoothing procedure, can be performed by using different free software, able to work with a single-surface triangulated mesh, such as Meshlab [54] or Meshmixer [55] by Autodesk®.
The solid geometry produced by means of the procedure illustrated in this Section is finally mesh discretized in space, to conduct FEM-based mechanical analyses on concrete asphalt.

3. Visco-elasto-plastic model

A coupled visco-elasto-plastic model is proposed to reproduce the mechanical behavior of the matrix material (bituminous binder), and its characteristic evolution in time under different loading conditions. A time-fractional non-local formulation is adopted for modeling the material visco-elasticity, as described in sub-section 3.1. A classic elasto-plastic formulation is used to model the unrecoverable strain evolution, as discussed in sub-section 3.2.
In sub-section 3.3 a possible coupling scheme between visco-elasticity and elasto-plasticity is finally proposed.

3.1. Visco-elastic formulation

Bituminous materials exhibit a time dependent mechanical behavior, which is influenced mainly by the load level, the loading time and

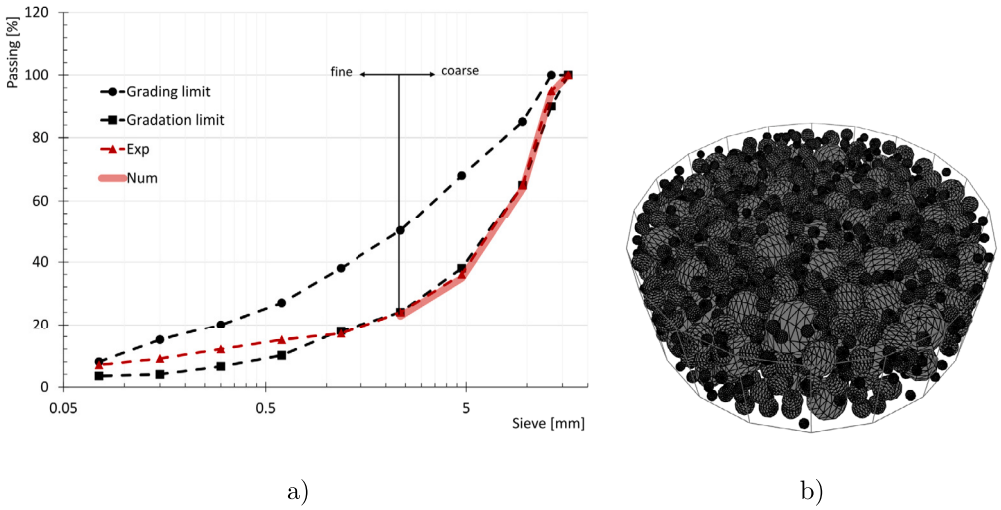

Fig. 2. Comparison between real [53] and simulated grading curve a); simulated random distribution of spherical inclusions in a cylindrical control volume b).

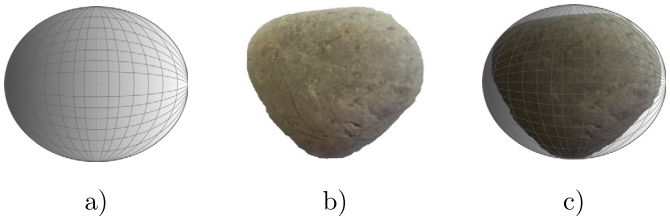

Fig. 3. Ideal ellipsoid shape a); example of a real aggregate shape b); ideal ellipsoid volume circumscribed to a real aggregate shape.

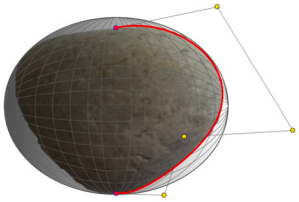

Fig. 4. Bézier -type approximation of a real aggregate shape in 2D space.

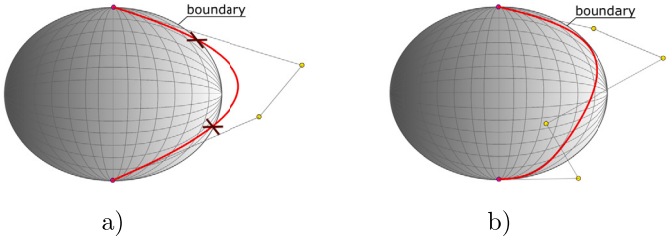

Fig. 5. Random positioning of the control points over the ideal ellipsoid surface: discarded configuration; a) admissible configuration b).

temperature. The adopted model for the visco-elastic formulation of the binder in the present work corresponds to the Modified Huet-Sayegh (MHS) fractional model [11,60]. The introduction of the fractional derivative mathematical operator in the constitutive law requires the development of appropriate computational strategies to be addressed in an efficient way [56–59]. The model itsef represents an upgrade to the original Huet-Sayegh (HS) model [10], for the additional linear dashpot in series with the HS unit (see Fig. 10). This accounts for an improved performance of the model itself in the low frequency region, when addressing visco-elasticity in the frequency domain [11]. Indeed, whereas the original model is characterized at the lower frequency region by a

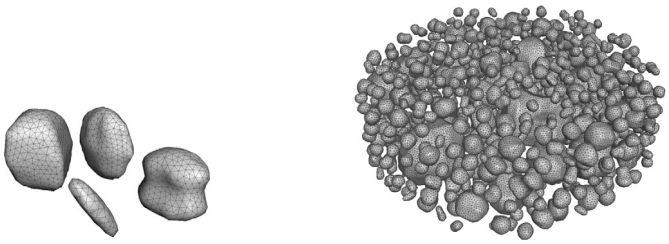

Fig. 6. Different aggregate realizations possible by adopting the Bézier approximation a); complete realization of a set of aggregates, randomly placed within a cyilindrical control volume and approximated in shape by adopting the Bézier technique b).

limiting non-zero rubbery shear modulus G_0, the MHS can approach a limiting value close to zero thanks to the additional dashpot element. As regards the HS unit, it consists in two parabolic dashpots placed in series with a linear spring operating at a shear modulus (G_∞-G_0), where G_∞ is the instantaneous shear modulus. G_∞ and G_0 represent the moduli at high frequency values (i.e. short loading times), and near zero frequency (i.e. very long loading times), respectively. This set is in parallel with another linear spring operating at the rubbery modulus of the material G_0. Based on the 1D rheological model in Fig. 10, the additive decomposition of the total visco-elastic strain ε^{ve} yields

$$\varepsilon^{ve} = \varepsilon^{e} + \left(\varepsilon^{1} + \varepsilon^{2} + \varepsilon^{LD}\right) = \varepsilon^{e} + \varepsilon^{v}, \tag{2}$$

where ε^{e} is the strain in the two parallel springs, $\varepsilon^{\mathrm{LD}}$ the strain in the linear dashpot, ε^{i} (with $i = 1, 2$) the strains in the parabolic dashpots, and ε^{v} the viscous part of the total visco-elastic strain.
The parabolic dashpot is described by the following fractional differential constitutive law in function of time t [8,9]

$$\sigma^{\mathrm{I}}(t) = \eta_i \tau_i^{m_i - 1} D^{m_i}_{t_0,t}[\varepsilon^{i}(t)]; \qquad i = 1, 2 \tag{3}$$

where η_i, τ_i and m_i are parameters of the parabolic dashpots; σ^{I} is the stress in the first branch of the MHS unit (see Fig. 10).
Specifically, the time constant τ_i is related to the damping coefficient η_i through the constant δ_i as

$$\delta_i = \frac{\tau_i (G_\infty - G_0)}{\eta_i}. \tag{4}$$

In Eq. (3) $D^{m_i}_{t_0,t}[f(t)]$ is the fractional operator of order $m_i \in \mathbb{R}^+$; $0 \leq m_i \leq 1$. The non-integer differential operator is a particularly versatile

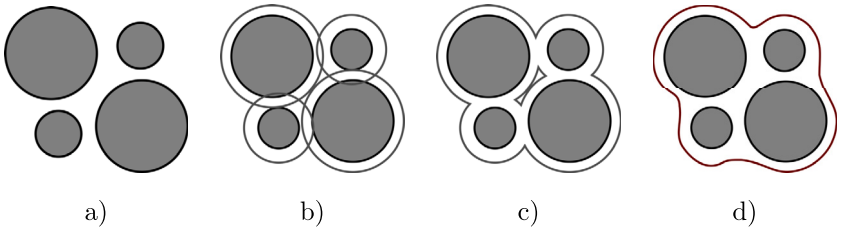

Fig. 7. Adopted procedure for matrix reconstruction in a 2D space, and for circular inclusions: initial configuration of randomly distributed inclusions a); offset around aggregates b); boolean operation between offset surfaces c); smoothing of surfaces d).

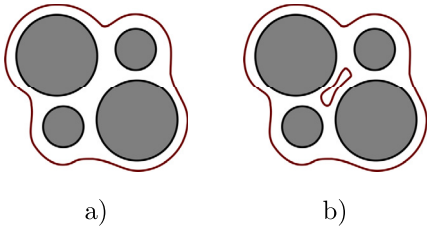

Fig. 8. Matrix reconstruction with different amount of surrounding binder material: without internal macroporosity a); with internal macroporosity b).

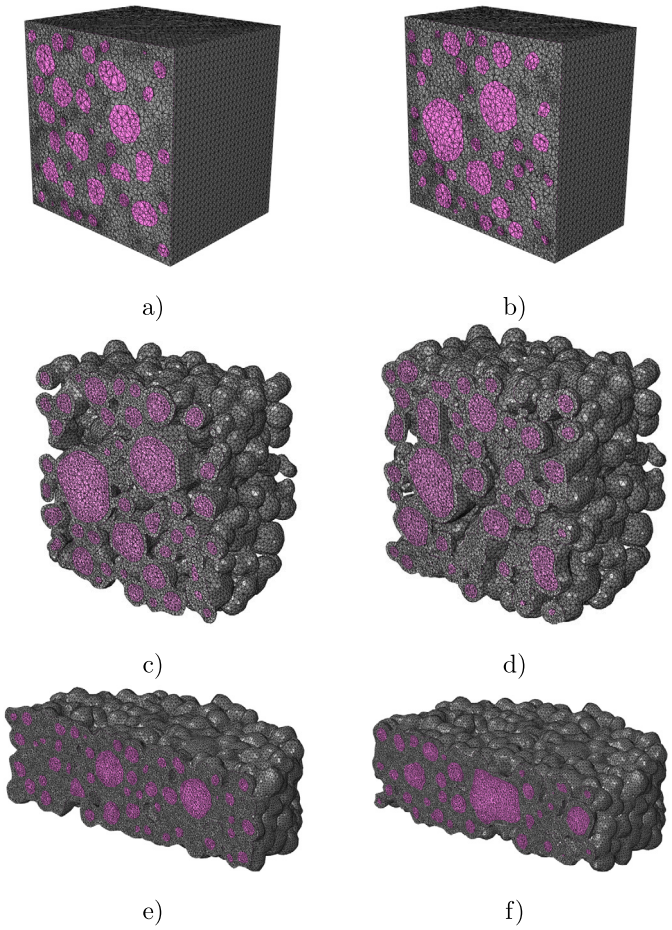

Fig. 9. Different solid geometries of a composite sample of concrete asphalt at the meso-scale reconstructed by using the proposed method, for different levels of internal macroporosity: cubic samples without internal macropores a), b); cubic samples with high internal macroporosity c), d); cylindrical sample with moderate internal macroporosity e), f).

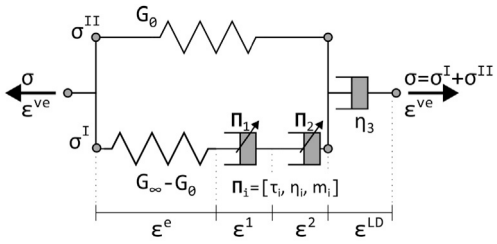

Fig. 10. The rheological Modified Huet-Sayegh visco-elastic model.

device in capturing visco-elasticity, by adjusting the material behavior as intermediate between a purely linear elastic behavior (for $m_i = 0$), and a purely linear viscous one (for $m_i = 1$). Various definitions exist in the literature for this mathematical operator [56,57]. The present work adopts the Grünwald-Letnikov (GL) representation, which is computationally efficient. In this context, the numerical approximation of the fractional term in this manner is extensively treated in [61,62]. By introducing the time discretization Δt, and by setting $t_0 = 0$, the fractional term can be construed as [61,62]

$$D^m_{t_0,t}[f(t)] = \lim_{\Delta t \to 0} \Delta t^{-m} \sum_{j=0}^{N} \mathrm{b}_j f(t - j\Delta t), \tag{5}$$

where the b_j coefficients can be recast in a recursive form by resorting to the properties of the Gamma function as

$$\mathrm{b}_j = \frac{\Gamma(j-m)}{\Gamma(-m)\Gamma(j+1)} = \frac{j-m-1}{j}\mathrm{b}_{j-1}; \qquad \mathrm{b}_0 = 1. \tag{6}$$

Clearly, in Eq. (6) it is: $(j - m - 1)/j < 1$, hence the fading memory feature of the fractional operator. Thus, the sum of terms in Eq. (5) can be conveniently truncated up to a value N, large enough to include all and only the first meaningful terms. In this manner, this sum handles the non-locality in time of the operator itself. From Eq. (5) and Eq. (3) a recursive definition for the strain components ε^1_{n+1} and ε^2_{n+1} at the parabolic dashpots is derived

$$\varepsilon^i_{n+1} = \frac{\Delta t^{m_i}}{\eta_i \tau_i^{m_i - 1}} \sigma^{\mathrm{I}}_{n+1} - \sum_{j=1}^{N} \mathrm{b}(m_i)_j \ \varepsilon^i_{n+1-j}. \qquad i = 1, 2 \tag{7}$$

It is noted from Eq. (7) that the calculation of the strain components pertaining to the parabolic dashpots requires the storage of the past strain history up to the N-th term for each fractional element. Different N values are generally required for different m order values of the parabolic dashpots. Under strain controlled conditions, an expression for the stress in the MHS unit is derived by considering Eq. (2) and Eq. (7) [30]. That is,

$$\sigma_{n+1} = \left[\frac{\chi}{1+\chi G_0} + \frac{\Delta t}{\eta_3}\right]^{-1} \cdot \left[\varepsilon^{ve}_{n+1} - \varepsilon^{\mathrm{LD}}_n + \frac{1}{1+\chi G_0}\left(\sum_{j=1}^{N} \mathrm{b}_j(m_1)\, \varepsilon^1_{n+1-j} + \sum_{j=1}^{N} \mathrm{b}_j(m_2)\, \varepsilon^2_{n+1-j}\right)\right], \tag{8}$$

in which the following parameter is introduced

$$\chi = \frac{1}{G_\infty - G_0} + \frac{\Delta t^{m_1}}{\eta_1 \tau_1^{m_1-1}} + \frac{\Delta t^{m_2}}{\eta_2 \tau_2^{m_2-1}}. \tag{9}$$

The strain of the linear dashpot is updated as

$$\varepsilon^{\mathrm{LD}}_{n+1} = \frac{\Delta t}{\eta_3}\sigma_{n+1} + \varepsilon^{\mathrm{LD}}_{n}. \tag{10}$$

For the generalization of the model in 3D space, the reader is referred to [30]. Further, the strain tensor and the stress tensor are divided into their deviatoric and hydrostatic part as

$$\boldsymbol{\sigma}_{n+1} = G\mathbf{M}_{\mathbf{G}}\boldsymbol{\varepsilon}^{ve}_{n+1} + K\mathbf{M}_{\mathbf{K}}\boldsymbol{\varepsilon}^{ve}_{n+1}, \tag{11}$$

where $\boldsymbol{\varepsilon}^{ve}$ is the visco-elastic strain tensor in Voigt notation; G and K are the shear and bulk modulus of the binder, respectively, and

$$\mathbf{M}_{\mathbf{G}} = \begin{pmatrix} \mathbf{S} & \mathbf{0} \\ \mathbf{0} & \mathbf{I} \end{pmatrix}; \qquad \mathbf{M}_{\mathbf{K}} = \begin{pmatrix} \mathbf{1} & \mathbf{0} \\ \mathbf{0} & \mathbf{0} \end{pmatrix} \tag{12}$$

are the dimensionless deviatoric and hydrostatic constitutive matrix, respectively; $\mathbf{0}$ is the zero 3 by 3 matrix, $\mathbf{I}$ the identity matrix, $\mathbf{1}$ the unit matrix, and $\mathbf{S}$ is defined as

$$\mathbf{S} = \begin{pmatrix} 4/3 & -2/3 & -2/3 \\ -2/3 & 4/3 & -2/3 \\ -2/3 & -2/3 & 4/3 \end{pmatrix}. \tag{13}$$

For asphalt mixture materials, studies by researchers [12,70] have demonstrated that under hydrostatic pressures typically experienced from tire contact stresses, the material exhibits a more pronounced time-dependent deformation behavior in shear than in the volumetric component. Consequently, the shear deformation component of the material is modeled as time-dependent, while the volumetric deformation component is treated as time-independent.

The adoption of an elastic bulk modulus and a viscoelastic shear modulus is widely accepted in modeling the response of asphalt concrete conglomerates [63]. Given the highly incompressible nature of bitumen, this approach provides a suitable representation, particularly for modeling the behavior of the binder [30]. Thus, in the proposed model it is assumed that the time dependent behavior applies solely to the shear modulus, G, while the bulk modulus, K, can be treated as time independent.

The material parameters in the 3D formulation are taken as

$$G_0 = \frac{3E_0K}{9K - E_0}; \qquad G_\infty = \frac{3E_\infty K}{9K - E_\infty}; \qquad \eta_{iG} = \frac{\eta_i}{3}; \qquad i = 1,2,3. \tag{14}$$

For modeling asphalt concrete response it is accepted that: $\delta_1 = \delta$ and $\delta_2 = 1$, in agreement with [10]. Thus, the material parameters of the MHS model can be reduced to 8 calibrating parameters: E_∞, E_0, the Poisson's ratio ν, m_1, m_2, $\tau_1 = \tau_2 = \tau$, δ_1 and the fading memory length N.

With the above simplifying assumptions, the visco-elastic stress can be obtained by generalization in 3D of Eq. (8) [30], that is

$$\boldsymbol{\sigma}_{n+1} = \left(\frac{\chi_G}{1+\chi_G G_0} + \frac{\Delta t}{\eta_{3G}}\right)^{-1}\left(\mathbf{M}_{\mathbf{G}}\boldsymbol{\varepsilon}^{ve}_{n+1} - \mathbf{M}_{\mathbf{G}}\boldsymbol{\varepsilon}^{\mathrm{LD}}_{n} + \Psi\right) + K\mathbf{M}_{\mathbf{K}}\boldsymbol{\varepsilon}^{ve}_{n+1} \tag{15}$$

with

$$\Psi = \frac{1}{1+\chi_G G_0}\left[\mathbf{M}_{\mathbf{G}}\sum_{j=1}^{N}\mathrm{b}_j(m_1)\,\boldsymbol{\varepsilon}^{1}_{n+1-j} + \mathbf{M}_{\mathbf{G}}\sum_{j=1}^{N}\mathrm{b}_j(m_2)\,\boldsymbol{\varepsilon}^{2}_{n+1-j}\right]. \tag{16}$$

The visco-elastic consistent tangent operator is obtained as [30]

$$\mathbf{C}^{ve} = \left[\frac{\chi_G}{1+\chi_G G_0} + \frac{\Delta t}{\eta_{3G}}\right]^{-1}\mathbf{M}_{\mathbf{G}} + K\mathbf{M}_{\mathbf{K}}, \tag{17}$$

where χ_G is derived from Eq. (9), by replacing to η η_G from Eq. (14). Finally, the viscous strain tensor at the current time step $\boldsymbol{\varepsilon}^{v}_{n+1}$ can be obtained as

$$\boldsymbol{\varepsilon}^{v}_{n+1} = \boldsymbol{\varepsilon}^{ve}_{n+1} - (\mathbf{C}^{ve})^{-1}\,\boldsymbol{\sigma}_{n+1}. \tag{18}$$

Table 1
Constitutive parameters used for the sensitivity analysis on parameter N: sample a) and sample b).

E_∞	180.00	MPa	E_∞	300.00	MPa
E_0	0.20	MPa	E_0	0.01	MPa
ν	0.40	MPa	ν	0.42	MPa
f_y	1.50	MPa	f_y	2.50	MPa
H^p	−0.50	MPa	H^p	−0.50	MPa
m_1	0.80		m_1	0.90	
m_2	0.30		m_2	0.40	
δ_1	0.80		δ_1	0.95	
δ_2	0.80		δ_2	0.95	
η_3	10×10^8		η_3	15×10^8	
τ_1	2.00	s	τ_1	1.50	s
τ_2	2.00	s	τ_2	1.50	s
a)			b)		

3.1.1. Parametric study of the truncation parameter N to approximate the fractional derivative term

The parameter N is the truncation value used to evaluate the fractional term in Eq. (5). By specifying the number of terms required to adequately approximate the fractional derivative within the GL representation, N essentially encapsulates the memory principle inherent in the fractional operator. While the determination of parameter N is contingent upon specific cases, exceeding a certain threshold value typically leads to solution stabilization.

To evaluate the solution's dependency on the selection of parameter N, a relaxation test is conducted numerically. Two distinct samples, labeled as a) and b) in Table 1, are simulated using different constitutive parameters, as delineated in Table 1. Beginning from an unloaded state (zero stress), a prescribed vertical displacement is applied to the samples, progressively increasing until a maximum vertical strain of $\varepsilon_{33} = 0.01$ is achieved over a duration of 12.5 s. Subsequently, the displacement is maintained constant, and the analysis is extended over a total duration of 500 s. N takes values in the range from 100 to 3500 for both samples (Fig. 11). Clearly, the variation in constitutive parameters yields distinct relaxation behaviors for the two samples, leading to corresponding changes in the solution at different values of N. Further, it is apparent from the same figure that the solution stabilizes for both samples when N exceeds 1500. Consequently, a value of $N = 2500$ has been selected for the numerical analyses conducted in this study.

3.2. Elasto-plastic formulation

For modeling the instantaneous plastic behavior of the binder material, an associative flow rule is considered [25]. Specifically, a rate independent Von Mises failure criterion is assumed, according to which the yield function in the stress space is defined as

$$f(\boldsymbol{\sigma}^p, \kappa) = \sqrt{3J_2'} - \sigma^y(\kappa) \le 0, \tag{19}$$

where $\boldsymbol{\sigma}^p$ is the instantaneous stress, J_2' the deviatoric stress second invariant; $\sigma^y(k) = \sigma^y_0 + H^p k$ is the yield stress in the case of linear isotropic hardening with constant hardening/softening modulus H^p, and κ is the adopted internal variable.

This formulation is particularly suitable for the limited number of required constitutive parameters. It is underlined that, without lack in generality, the proposed visco-elasto-plastic model can handle more complex elasto-plastic models.

In the assumption of an associative flow rule, the evolution of the plastic strain $\boldsymbol{\varepsilon}^p$ is evaluated in function of a plastic potential g equal to the yield function $f(\boldsymbol{\sigma}^p, \kappa)$ as

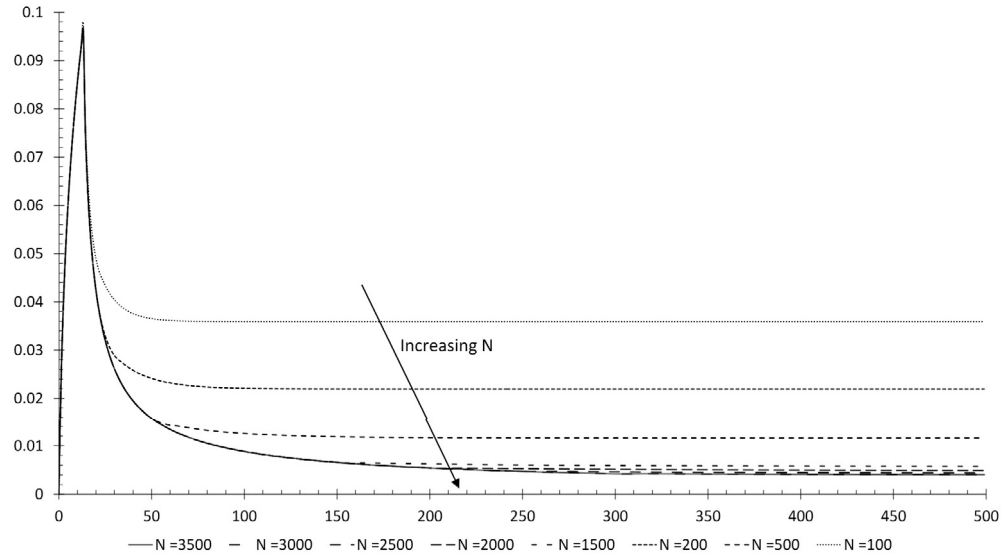

a)

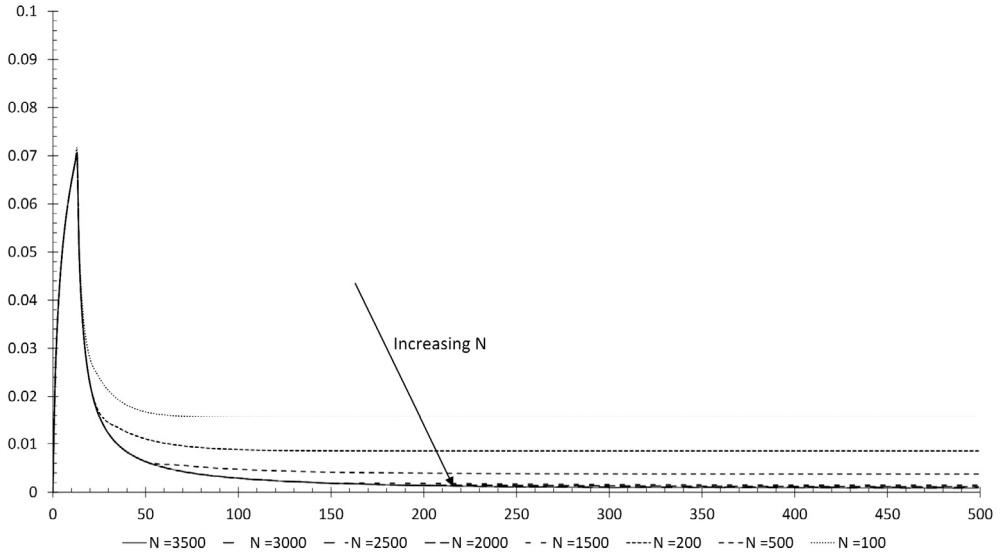

b)

Fig. 11. Results of relaxation tests performed at varying values of N for sample a) and sample b).

$$\dot{\boldsymbol{\varepsilon}}^p = \gamma \frac{\partial g}{\partial \boldsymbol{\sigma}^p}, \tag{20}$$

where γ is the plastic multiplier. The evolution in time of the internal variable is evaluated as

$$\dot{\kappa} = \int_0^t \sqrt{\frac{2}{3}} ||\dot{\boldsymbol{\varepsilon}}^p|| dt \tag{21}$$

in agreement with [64].

The elasto-plastic problem is solved by using the classical elastic predictor- plastic corrector scheme. Specifically, a trial stress is assumed as

$$\boldsymbol{\sigma}_{n+1}^{Tr} = \mathbf{C}(t_n)\,\boldsymbol{\varepsilon}_{n+1}^{ve,Tr} = \mathbf{C}\left(\boldsymbol{\varepsilon}_{n+1} - \boldsymbol{\varepsilon}_n^p\right), \tag{22}$$

where $\mathbf{C}(t_n) = \mathbf{C}$ is the elastic constitutive tensor at time t_n, and $\boldsymbol{\varepsilon}^{ve,Tr}$ is the trial visco-elastic strain tensor. Next, the return mapping (RM) scheme is performed to correct the trial stress if the plastic check $f(\boldsymbol{\sigma}_{n+1}^{Tr}, \kappa_n) \leq 0$ fails. This leads to the solution of the non-linear system

$$\mathbf{b} = \begin{cases} f(\boldsymbol{\sigma}_{n+1}^p, \kappa_{n+1}) = 0 \\ \mathbf{r} = \boldsymbol{\sigma}_{n+1}^p - \boldsymbol{\sigma}_{n+1}^{Tr} + \mathbf{C}\dot{\boldsymbol{\varepsilon}}^p{}_{n+1} = \mathbf{0}, \\ h = \kappa_{n+1} - (\kappa_n + \dot{\kappa}) \end{cases} \tag{23}$$

which is solved by using the Newton-Raphson method. After introducing the state variable vector $\mathbf{x} = [\boldsymbol{\sigma}, \gamma, \kappa]^T$, the RM scheme can be recast into

$$\mathbf{x}^{m+1} = \mathbf{x}^m - \mathbf{A}^{-1}\mathbf{b}, \tag{24}$$

where $\mathbf{A}$ is the matrix of the linearized system, that is

$$\mathbf{A} = \begin{bmatrix} \frac{\partial f}{\partial \boldsymbol{\sigma}} & \frac{\partial f}{\partial \gamma} & \frac{\partial f}{\partial \kappa} \\ \frac{\partial \mathbf{r}}{\partial \boldsymbol{\sigma}} & \frac{\partial \mathbf{r}}{\partial \gamma} & \frac{\partial \mathbf{r}}{\partial \kappa} \\ \frac{\partial h}{\partial \boldsymbol{\sigma}} & \frac{\partial h}{\partial \gamma} & \frac{\partial h}{\partial \kappa} \end{bmatrix}. \tag{25}$$

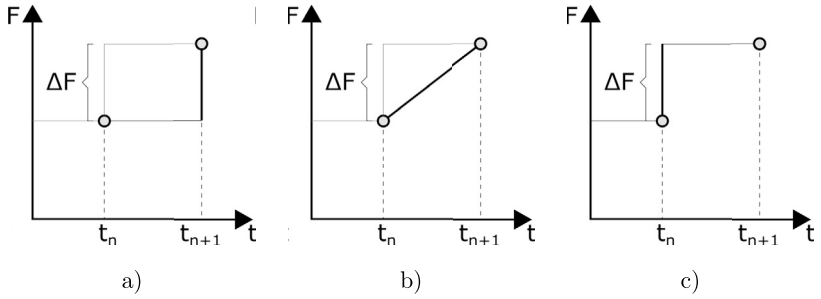

Fig. 12. Numerical scheme of possible application of the load increment in a transient solver for conducting transient mechanical analyses: at the end of the time step a); continuously (linearly) within the time step b); at the beginning of the time step c).

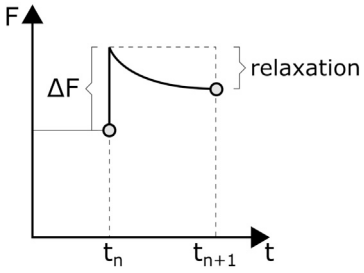

Fig. 13. Adopted numerical scheme for the application of the load increment, and subsequent evolution of stress relaxation.

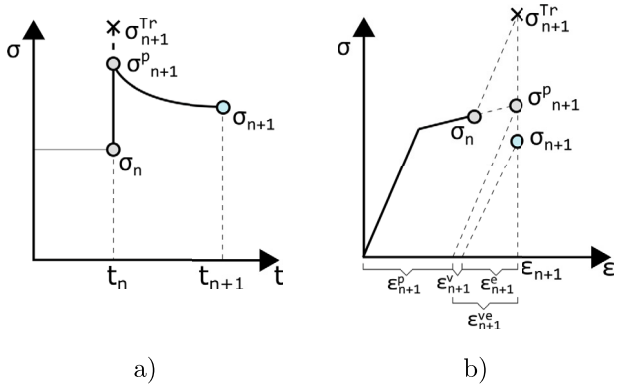

Fig. 14. Return mapping scheme: stress versus time a), and stress versus strain b).

Finally, the consistent tangent operator for the elasto-plastic model is construed in agreement with [65]

$$\mathbf{C}^{ep} = \frac{\partial \Delta \boldsymbol{\sigma}^{p}_{n+1}}{\partial \boldsymbol{\varepsilon}_{n+1}} = \mathbf{A}_{12}^{-1}\mathbf{C}. \tag{26}$$

3.3. Coupling between creep and elasto-plasticity

The classical implementation of a non-linear transient solver operating in the mechanical field demands that the equilibrium solution is reached at each time step in which time is discretized. The equilibrium condition at a current time step t_{n+1} is met by setting close to zero the residual between the external and the internal forces computed at the specific time step, that is

$$\hat{\mathbf{r}}(t_{n+1}) = \mathbf{F}^{ext}(t_{n+1}) - \mathbf{F}^{int}(t_{n+1}). \tag{27}$$

It is observed that the load increment ΔF can be applied in different manners within the time interval $[t_n\ t_{n+1}]$: at the end of the time step (Fig. 12 a)); continuously (linearly) within the time step (Fig. 12 b)), or instantaneously at the beginning of the time step (Fig. 12 c)). In the present work the load increment is assigned instantaneously at the beginning of each time step, as indicated in Fig. 12 c). Thus, after the instantaneous application of the loading, it is assumed that the long-term effects associated to creep evolution in time take place (see Fig. 13). The adoption of this specific numerical scheme implies that at the current time step t_{n+1} the elasto-plastic stress is defined based on the visco-elastic stress evaluated at the previous time step t_n. Next, the new visco-elastic stress is estimated at time t_{n+1} through the creep model discussed in subsection 3.1.

Introduce the additive decomposition of the total strain tensor $\boldsymbol{\varepsilon}$

$$\boldsymbol{\varepsilon}_{n+1} = \boldsymbol{\varepsilon}_n + \Delta\boldsymbol{\varepsilon} = \boldsymbol{\varepsilon}^{e}_{n+1} + \boldsymbol{\varepsilon}^{v}_{n+1} + \boldsymbol{\varepsilon}^{p}_{n+1} = \boldsymbol{\varepsilon}^{ve}_{n+1} + \boldsymbol{\varepsilon}^{p}_{n+1}. \tag{28}$$

Thus, the trial elastic stress for the coupled visco-elasto-plastic model is defined as

$$\boldsymbol{\sigma}^{Tr}_{n+1} = \boldsymbol{\sigma}_n + \mathbf{C}^{ve}(t_n)\Delta\boldsymbol{\varepsilon}, \tag{29}$$

where $\mathbf{C}^{ve}$ takes the expression in Eq. (17).

The RM is performed if the plastic check fails. The RM scheme moves the trial stress into the yield surface and the instantaneous stress tensor $\boldsymbol{\sigma}^{p}_{n+1}$ is obtained by solving Eq. (24), as shown in Fig. 14. After the plastic correction, the current stress $\boldsymbol{\sigma}_{n+1}$ is finally obtained from Eq. (15).

The visco-elasto-plastic consistent tangent operator $\mathbf{C}^{vep}$ is obtained starting from Eq. (28). Hence, by using the chain rule, yields

$$\mathbf{C}^{vep} = \frac{\partial \boldsymbol{\sigma}_{n+1}(\boldsymbol{\varepsilon}^{ve}_{n+1})}{\partial \boldsymbol{\varepsilon}_{n+1}} = \mathbf{C}^{ve}\frac{\partial \boldsymbol{\varepsilon}^{ve}_{n+1}}{\boldsymbol{\varepsilon}_{n+1}}, \tag{30}$$

where $\mathbf{C}^{ve} = \dfrac{\partial \boldsymbol{\sigma}_{n+1}(\boldsymbol{\varepsilon}^{ve}_{n+1})}{\partial \boldsymbol{\varepsilon}^{ve}_{n+1}}$ is the consistent tangent operator of the visco-elastic model computed by using Eq. (17).

Further, the current visco-elastic strain $\boldsymbol{\varepsilon}^{ve}_{n+1}$ is a function of the plastic strain computed at the beginning of the time step, $\boldsymbol{\varepsilon}^{p}_{n}$, that is,

$$\boldsymbol{\varepsilon}^{ve}_{n+1} = \boldsymbol{\varepsilon}_{n+1} - \boldsymbol{\varepsilon}^{p}_{n+1} = \boldsymbol{\varepsilon}_{n+1} - \boldsymbol{\varepsilon}^{p}_{n} - \gamma\frac{\partial g}{\partial \boldsymbol{\sigma}^{p}_{n+1}}. \tag{31}$$

The first derivative of $\boldsymbol{\varepsilon}^{ve}_{n+1}$ over the total strain is derived as

$$\frac{\partial \boldsymbol{\varepsilon}^{ve}_{n+1}}{\boldsymbol{\varepsilon}_{n+1}} = \mathbf{I} - \gamma\frac{\partial^2 g}{\partial \boldsymbol{\sigma}^{p\,2}_{n+1}}\frac{\partial \boldsymbol{\sigma}^{p}_{n+1}}{\partial \boldsymbol{\varepsilon}_{n+1}} = \mathbf{I} - \gamma\frac{\partial^2 g}{\partial \boldsymbol{\sigma}^{p\,2}_{n+1}}\mathbf{C}^{ep}, \tag{32}$$

with $\mathbf{C}^{ep}$ elasto-plastic consistent tangent operator, defined in Eq. (26). After manipulation of Eq. (31) and Eq. (32), the consistent tangent operator for the coupled visco-elasto-plastic can be written as

$$\mathbf{C}^{vep} = \mathbf{C}^{ve}\left(\mathbf{I} - \gamma\frac{\partial^2 g}{\partial \boldsymbol{\sigma}^{p\,2}_{n+1}}\mathbf{C}^{ep}\right). \tag{33}$$

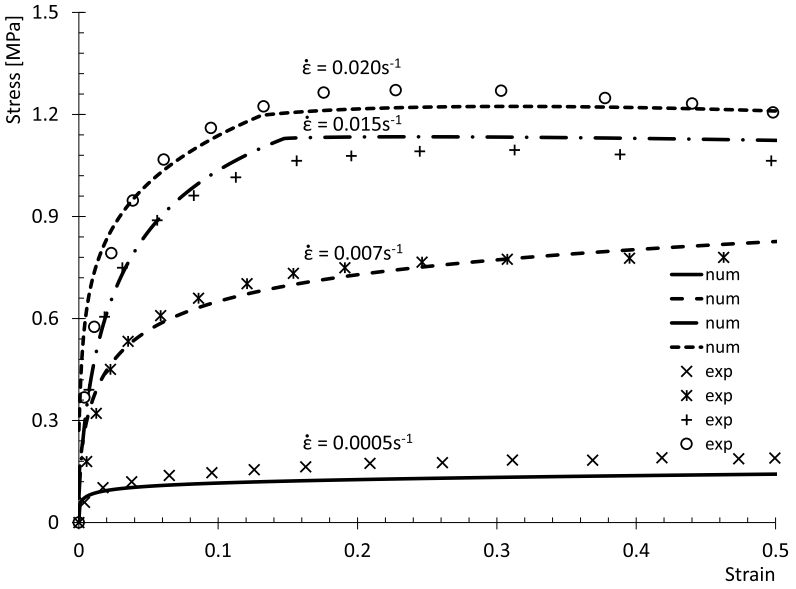

Fig. 15. Constant strain-rate tests: comparison between experimental [66] and numerical results.

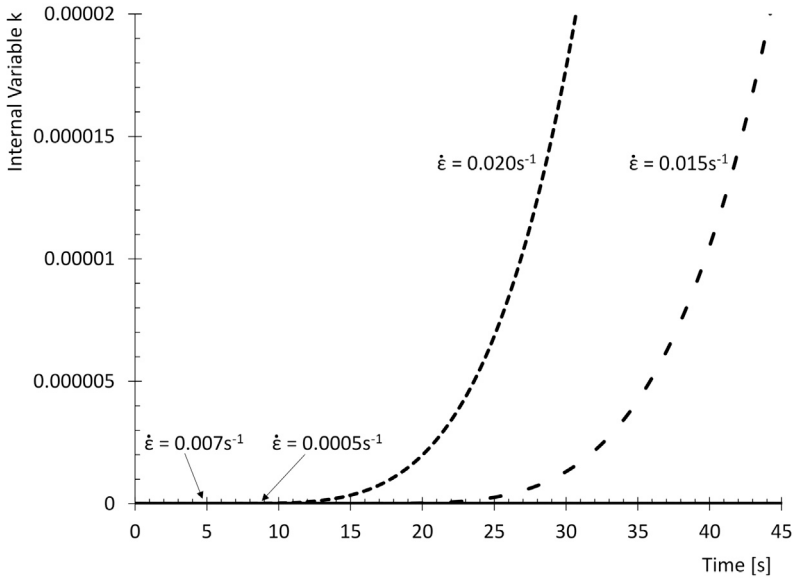

Fig. 16. Constant strain-rate tests: evolution of the plastic strain in the numerical results.

4. Results and discussion

4.1. Calibration of the visco-elasto-plastic model

The proposed constitutive model for the binding constituent of asphalt concrete has been calibrated and validated against the experimental tests reported in [66]. As a first example, the performance of the model in reproducing tests in which the strain rate is maintained constant in the sample, is analyzed. In these tests dumbbell-shaped samples have been loaded with a constant axial strain rate $\dot{\epsilon}$. In Fig. 15 the comparison between the experimental and the numerical results is shown for a 50 penetration grade bitumen at 0 °C for four different values of the applied strain rate.

The numerical parameters used to calibrate the curve characterized by $\dot{\epsilon} = 0.015\ s^{-1}$ are reported in Table 2. The other sets of data are used for validation of the proposed constitutive model by maintaining the same material parameters identified with the calibration procedure, and by simply varying the strain rate applied to the sample ($\dot{\epsilon} = 0.007\ s^{-1}$, $\dot{\epsilon} = 0.0005\ s^{-1}$) and $\dot{\epsilon} = 0.02\ s^{-1}$.

Table 2
Constitutive parameters used for calibration and validation of the model in relation to constant strain rate tests on samples made by a 50 penetration grade bitumen at 0 °C [66].

E_∞	200.00	MPa	E_0	0.20	MPa
ν	0.40	MPa			
f_y	1.80	MPa	H^p	−0.80	MPa
m_1	0.92		m_2	0.34	
δ_1	0.92		δ_2	0.92	
η_3	12.1×10^8				
τ_1	2.00	s	τ_2	2.00	s

Fig. 16 shows the evolution of the internal variable κ, adopted in the elasto-plastic formulation (Eq. (19)), in the sample for each applied strain rate. From this plot it is found that the sample undergoes irreversible inelastic strains during creep for $\dot{\epsilon} = 0.015$ and $0.02\ s^{-1}$.

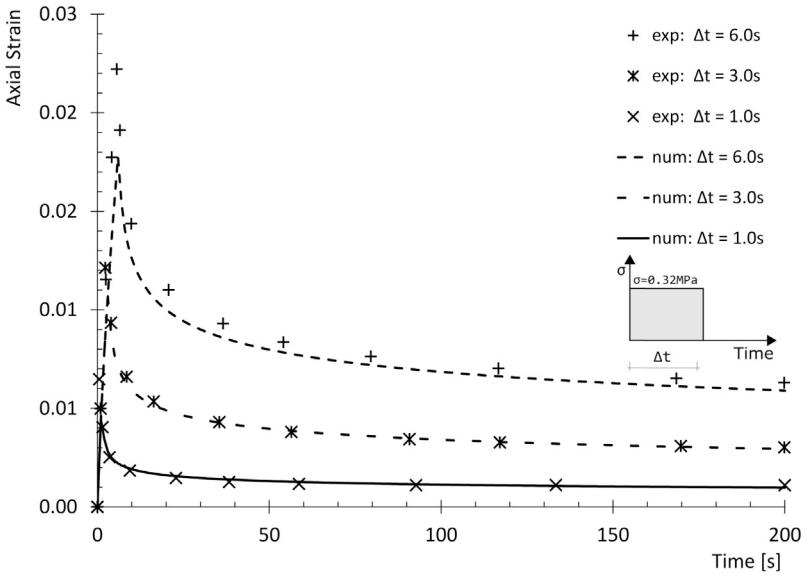

Fig. 17. Constant stress tests/creep recovery tests: comparison between experimental [66] and numerical results.

Table 3
Constitutive parameters used for calibration and validation of the model in relation to constant stress tests/creep recovery tests on samples made by a 50 penetration grade bitumen at 10 °C [66].

E_∞	160.00	MPa	E_0	0.20	MPa
ν	0.40	MPa			
f_y	1.80	MPa	H^p	−0.80	MPa
m_1	0.82		m_2	0.24	
δ_1	0.92		δ_2	0.92	
η_3	12.1×10^8				
τ_1	2.00	s	τ_2	2.00	s

As a second example, creep recovery tests on the same 50 penetration bitumen material have been considered. Specimens were tested at 10 °C, under a constant axial stress $\sigma = 0.32$ MPa. After the application of the load, the bitumen was allowed to creep to a specified total nominal tensile strain until release of the applied stress. Different loading times were considered in the experiment: 6.0 s, 3.0 s and 1.0 s.
The comparison between the experimental and numerical results is shown in Fig. 17. Similarly as before, one experimental data set has been used for calibration of the bitumen material parameters; the other two data sets account for validation of the proposed model. The material parameters identified for this test set-up are reported in Table 3. It is noted that some constitutive parameters required further recalibration with respect to the previous example. This is because this second series of tests was conducted at a different temperature.
After calibrating the mechanical behavior of bitumen, the model is used to conduct meso-mechanical studies in the next Section.

4.2. Meso-scale model

The performance of the proposed constitutive model for bituminous materials has been assessed at the meso-scale by reproducing at this scale the experimental tests on concrete asphalt reported in [67]. The tested specimens are cylindrical, 10 mm in diameter and 20 mm height, with composition and grading as reported in Table 4. The procedure described in Section 2 has been adopted to reconstruct a numerical sample in line with the given composition and grading curve. Practically, the coarse aggregate fraction in the range [1.18 − 2.36] mm has been explicitly modeled, while the fine fraction has been considered as part of the matrix phase, together with the binding bituminous material. The simulated composition is summarized in Table 5. In the same Table the percentage variation between the real and the simulated volume fraction is also reported. In Fig. 18 the reconstructed geometry of one sample is shown, distinguished into matrix phase (Fig. 18 a)) and coarse aggregates (Fig. 18 b)). A section of the assembled model is shown in Fig. 18 c), where aggregate inclusions and macropores are visible. In the experimental test reported in [67] the sample was constrained at the top and bottom faces by a press machine, while being subjected to a random compressive loading. The load was applied at a velocity of 0.25 mm/s, and randomly in loading level and duration, as reported in the loading scheme of Fig. 19 a). This reflects on the asphalt material as a random duration of creep, and of creep recovery. In this scenario the asphalt concrete sample is expected to exhibit a visco-elasto-plastic behavior in time corresponding to a series of subsequent creep recovery tests of different loading levels and duration. The test was conducted at a temperature of 20 °C.
To calibrate the material constitutive parameters of the binder, an iterative process was employed to find the optimal set of calibration values. This process aimed to ensure that the axial strain history in the sample, resulting from the random loading protocol, closely matched the empirical data for the initial two loading cycles of the test. Consequently, the alignment between numerical and experimental results in subsequent load cycles is attributable to the calibration performed during the initial cycles.
The calibrating material parameters for the proposed visco-elasto-plastic constitutive model attributed to the matrix phase are reported in Table 6. Aggregates have been assumed to behave as linearly elastic, with Young's modulus $E = 80000$ MPa [72] and Poisson's ratio $\nu = 0.2$ [71].

The comparison between experimental and numerical results of the cyclic random loading test is shown in Fig. 19 b) in terms of axial strain in the sample versus time. A fairly good agreement is observed between the experimental results and results obtained by using the proposed numerical visco-elasto-plastic model for the binder. In the same figure, it can be observed that the alignment between the results is slightly more precise for the initial load cycles compared to the final ones. This discrepancy stems from the calibration procedure, which was limited to the first two loading cycles, with the subsequent data being predicted numerically by the model.
Interestingly, when analyzing the mechanical behavior of asphalt concrete at the scale of its constituents, local effects of material plasticization are captured. They are generated by the interaction between matrix and inclusions during the loading process, due to their different stiffness. The observed phenomena can be explained by the localized stress increments caused by inclusions within the binder matrix, which are further

Table 4
Composition of asphalt concrete samples considered for the numerical analyses at the meso-scale [67,68].

	fine inclusions	coarse inclusions	bitumen	air void
size [mm]	0.15 - 0.3	1.18 - 2.36		
density [t/m^3]	2.69×10^{-9}	2.67×10^{-9}	1.03×10^{-9}	
volume fraction [%]	37.5	37.5	21.0	4.0

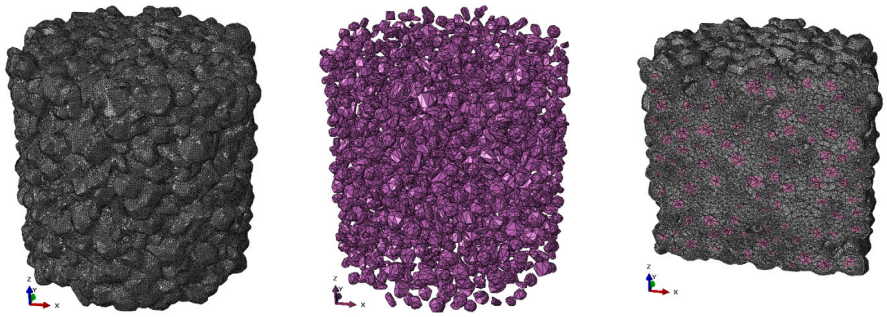

a) b) c)

Fig. 18. Reconstructed meso-scale sample: matrix a); inclusions b); vertical section of assembled sample c).

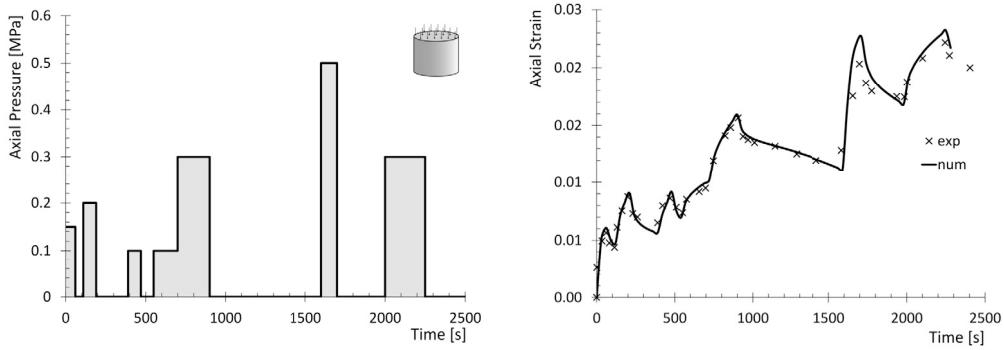

a) b)

Fig. 19. Loading scheme of the random loading creep test reported in [67] a); comparison between experimental [67] and numerical results b).

Table 5
Simulated composition of the asphalt concrete samples reported in [67], considered for the numerical analyses at the meso-scale.

	coarse inclusions	matrix	air void
size [mm]	1.18 - 2.36		
volume fraction [%]	36.9	59.0	4.1
exp.-num. variation [%]	1.5	0.8	1.8

Table 6
Constitutive parameters used for the matrix in simulating the random loading creep test reported in [67].

E_∞	106.00	MPa	E_0	0.08	MPa
ν	0.35	MPa			
f_y	0.90	MPa	H^p	−0.80	MPa
m_1	0.60		m_2	0.17	
δ_1	0.59		δ_2	0.19	
η_3	12.1×10^8				
τ_1	30.25	s	τ_2	30.26	s

compounded by their irregular geometries, resulting in non-uniform stress distributions. In Fig. 20 contour maps of the accumulated inelastic strains at the end of the loading process are plotted. It is observed that locally, around the aggregates, the adopted nonlinear material modeling leads to the development of not recoverable strains during creep evolution.

The primary advantage of meso-scale modeling lies in its capability to accurately characterize localized irreversible strains by considering interactions between the aggregates. This allows for the evaluation of local behaviors that are not numerically visible when employing a macroscopic approach.

4.3. Indirect tensile strength test for asphalt emulsion

Asphalt emulsion mixtures comprise asphalt emulsion (a blend of asphalt cement, water, and emulsifying agents) mixed with aggregates (such as sand, gravel, or crushed stone) and other additives. They are typically manufactured and applied at lower temperatures compared to hot mix asphalt. Following the experimental protocol delineated in [69], Indirect Tensile Strength (ITS) tests were conducted in accordance with ASTM D6931-12 standard. The tests utilized samples with a diameter of 101.6 mm, a loading strip width of 12.7 mm, and a loading

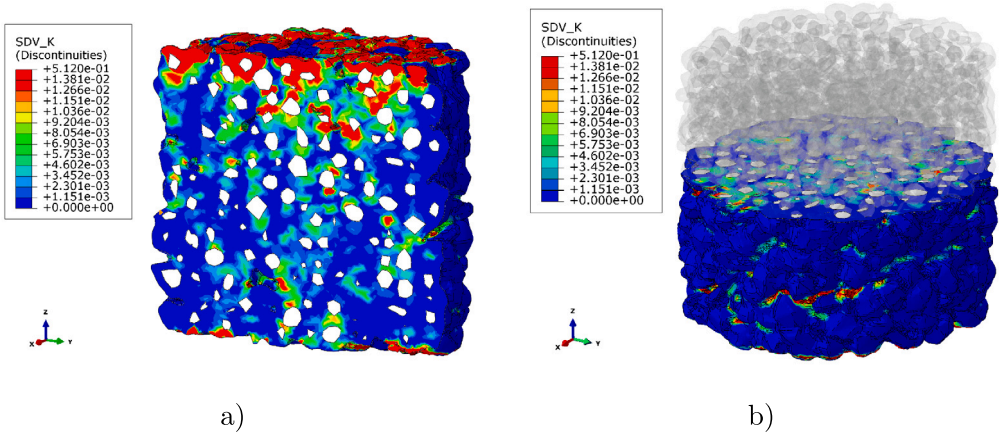

Fig. 20. Inelastic strains in the sample at the end of the random loading creep test [67]: vertical section a); transversal section b) of the sample.

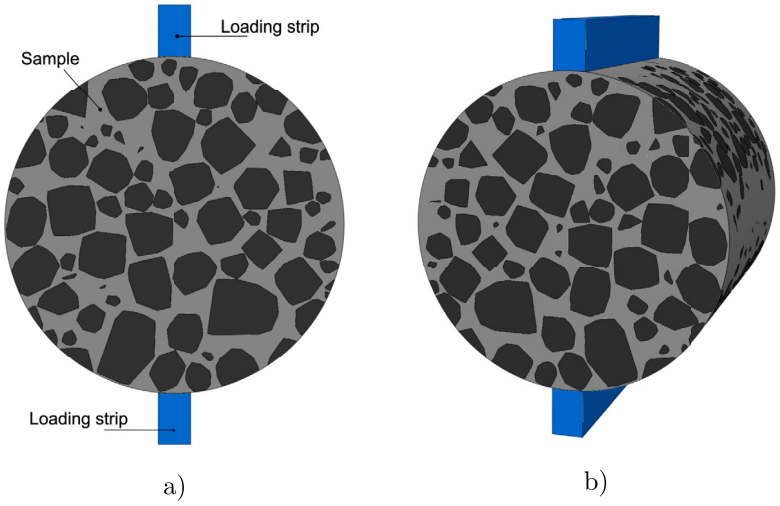

Fig. 21. Numerical model of the ITS test on an asphal emulsion sample: front view a); axonometric view b).

Table 7
Coarse aggregates grading.

	Passing percentage of sieve [mm]				
	20	16	13.2	9.5	4.75
Loss [%]	100	95	84	78	48

rate of 50 mm/s. The grading curve utilized in specimen production is presented in Table 7. This grading curve was reconstructed numerically using the random distribution algorithm detailed in Subsection 2.1. Polyhedral shapes were chosen for the inclusions due to their alignment with the geometric characteristics of the aggregates within the tested samples (Fig. 21).

The reconstruction of coarse aggregates within the 3D model is depicted in Fig. 22, highlighting the polyhedral shape specifically adopted. In the geometrical reconstruction, the sample is assumed to be dense, devoid of macro-porosity, with pore dimensions considered to be less than 5 mm. Consequently, these pores are homogenized into the matrix, mirroring the treatment of finer particles in the grading curve (aggregates with nominal diameters less than 5 mm are not individually modeled but are assimilated into the matrix). The experimental tests proposed by Mahyuddin et al. [69] involved the addition of varying proportions of natural rock (Buton Granular Asphalt, BGA) to a base mix, aimed at enhancing the material's strength performance. Specifically, Indirect Tensile Strength (ITS) tests were conducted to assess the increase in tensile strength attributable to the additive. The experimental campaign encompassed three distinct BGA percentages: 2.5%, 5.0%, and 7.5%. The relationship between yield stress and BGA percentage was determined through polynomial interpolation of the experimental data, as follows

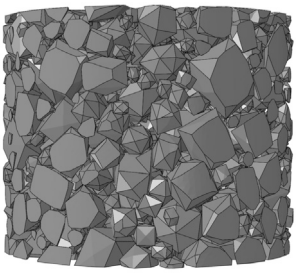

Fig. 22. Aggregates reconstruction in the sample used for the ITS test.

$$\frac{f_y}{f_{y0}} = a + \psi\left[b + \psi\left(c + d\psi\right)\right], \tag{34}$$

where ψ represents the percentage of BGA in the mix, and the constants $[a, b, c, d]$ of the interpolating curve are listed in Table 23 a). By employing this simplified data extrapolation method, it is anticipated that the polynomial curve depicted in Fig. 23 b) will align with experimental ob-

a	b	c	d
1.00	55.83	−818.48	4163.20

a)

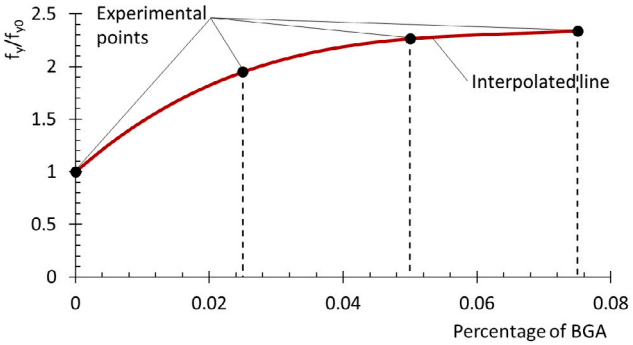

b)

Fig. 23. Polynomial parameters a); interpolating curve of experimental results reported in [69] b).

Table 8
Constitutive parameters used to simulate the ITS test proposed in [69].

E_∞	120	MPa	E_0	10.5	MPa
ν	0.35		f_{y0}	0.95	MPa
f_y	Eq. (34)		H^p	−9.5	MPa
m_1	0.9		m_2	0.32	
δ_1	0.91		δ_2	0.91	
δ_3	12.1×10^8				
τ_1	30	s	τ_2	30	s

servations within the limited range of BGA percentages tested, namely: $[0\%, 7.5\%]$.
For the numerical reproduction of the ITS test the constitutive parameters shown in Table 8 have been adopted. Specifically, f_y has been assumed in agreement with Eq. (34).
The aggregates have been characterized by a Young's modulus equal to 55000 MPa and a Poisson's ratio equal to 0.15.
Fig. 24 illustrates the comparison between experimental and numerical stress-strain curves for the tested samples at varying BGA percentages examined in the experiment. The numerical results are found in good agreement with the experimental findings. This analysis underscores the capacity of the proposed model to accurately capture the macroscopic material nonlinearity displayed by the asphalt mixture across different BGA percentages. Fig. 25 presents the evolution of the plastic internal variable at various analysis times for a representative cross-section of the sample. It is noteworthy that other cross-sections within the sample exhibit a similar behavior (not depicted here for brevity). The initiation of plastic strains occurs at the loading strip and progresses with the loading increments along the diametral direction. Furthermore, Fig. 25 illustrates that plastic strains are induced in the interstices between aggregates, contributing to stress concentration.

5. Conclusions

In this paper a 3D visco-elasto-plastic model for bituminous materials is proposed finding use in concrete asphalt production. The model adopts a fractional approach for the visco-elastic part, which is implemented in line with the modified Huet-Sayegh model. Further, plasticity is addressed under the assumption of an associative flow rule for the plastic strain component. A coupling scheme between visco-elasticity and plasticity is proposed, and small strains are considered. By using the chain rule, the visco-plastic and the visco-elasto-plastic consistent tangent operators are construed.
For a realistic modeling of asphalt concrete specimens at the meso-scale, a random distribution algorithm is developed and used to place aggregate inclusions in a reference volume, compliant with assigned grading curve and assigned coarse aggregate volume fraction. Further, it is proposed that the solid modeling is enriched by: i) a geometrical approximation of the outer surface of aggregate inclusions through Bézier parametric splines, and ii) the performing of boolean operations between offset surfaces, to generate a matrix phase compatible with a given macroporosity degree of the binder.
By juxtaposition of numerical results versus experimental creep tests of different nature and indirect tensile strength tests, the model demonstrates robust predictive capabilities. Specifically, it allows to capture the evolution of visco-elastic strains and to anticipate the onset of inelastic strains at the meso-scale.
There is potential for further enhancement of the model by considering the influence of asphalt material behavior under non-ambient temperature conditions.
In conclusion, the main advantages of the proposed approach can be summarized in the possibility: i) to combine a model visco-elasticity based on a fractional derivative formulation with plasticity, to capture the inelastic strain evolution during creep of asphalt materials, ii) to conduct meso-mechanical studies on a realistic 3D geometry of the composite, iii) to investigate complex three-axial stress states, close to the material admissible strength, and taking into account confinement.
All these aspects coexist in the formulation proposed in this work for the study of bituminous materials at the scale of individual constituents, aiming to provide the most comprehensive and all-encompassing approach to the problem under examination.

CRediT authorship contribution statement

G. Mazzucco: Writing – review & editing, Writing – original draft, Visualization, Validation, Supervision, Software, Project administration, Conceptualization. **B. Pomaro:** Writing – review & editing, Writing – original draft, Visualization, Validation, Supervision, Conceptualization. **V.A. Salomoni:** Writing – review & editing, Resources. **C.E. Majorana:** Writing – review & editing, Resources, Funding acquisition.

Declaration of competing interest

The authors declare that they have no known competing financial interests or personal relationships that could have appeared to influence the work reported in this paper.

Data availability

Data will be made available on request.

Acknowledgements

The financial support from the Italian Ministry of University and Research (MUR), in the framework of PRIN2017 Project 2017HFPKZY, PRIN2020 Project 20209F3A37 and PRIN2022 Project P2022BTAPP is gratefully acknowledged.

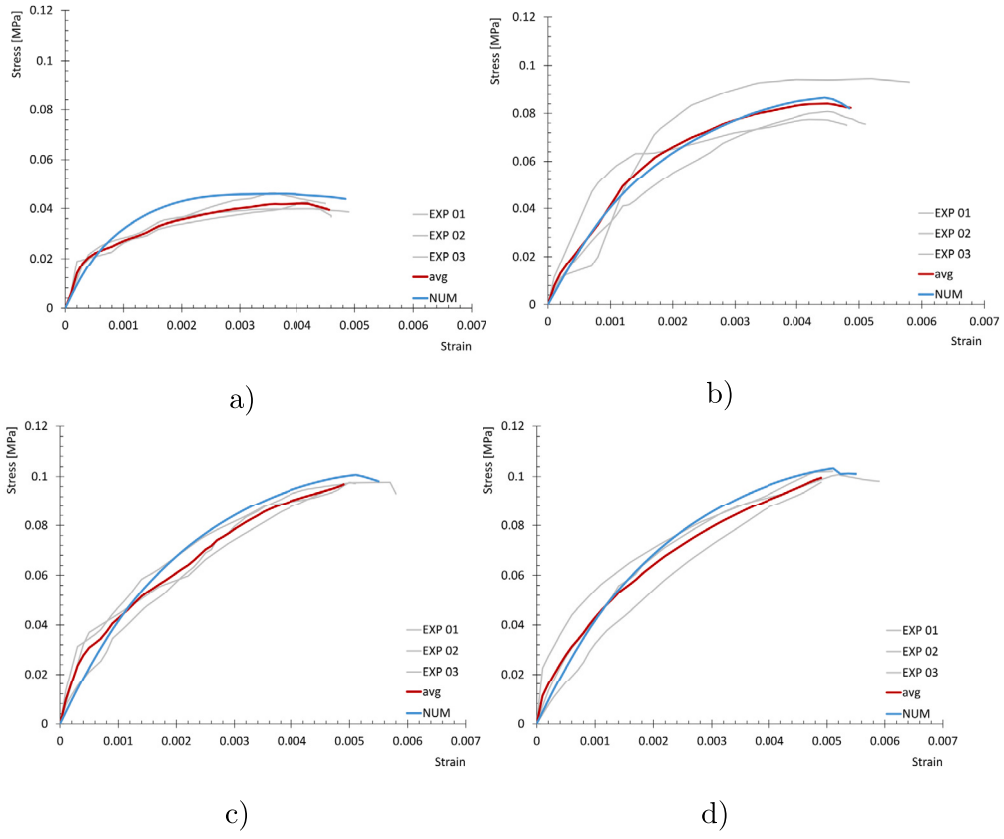

Fig. 24. Comparisons of stress vs. strain curves from experimental [69] and numerical results at different asphalt natural rock percentages: 0% of BGA a); 2.5% of BGA b); 5.0% of BGA c) and 7.5% of BGA d).

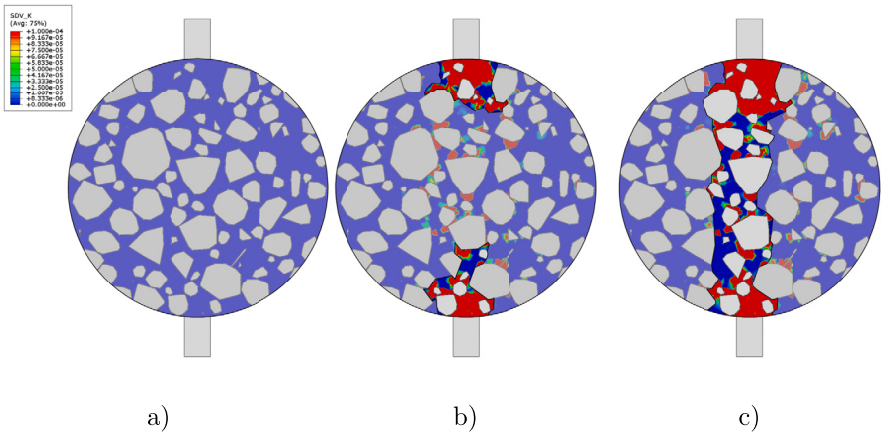

Fig. 25. Material failure evolution at different load increments: no load a) at halfway through the analysis b); at failure (end of analysis and of the ITS test) c).

References

[1] Rothenburg L, Bogobowicz A, Haas R, Jung RW, Kennepohl G. Micromechanical modelling of asphalt concrete in connection with pavement rutting problems. In: Proceedings of the seventh international conference on the structural design of asphalt pavements; 1992.

[2] Papagiannakis A, Abbas A, Masad E. Micromechanical analysis of viscoelastic properties of asphalt concretes. Transp Res Rec 2002;1789:113–20.

[3] Sadd MH, Dai Q, Parameswaran V, Shukla A. Microstructural simulation of asphalt materials: modeling and experimental studies. J Mater Civ Eng 2004;16(2):107–15.

[4] Kringos N, Scarpas A, Kasbergen C. Three-dimensional elasto-visco-plastic finite element model for combined physical-mechanical moisture induced damage in asphalt mixes. J Assoc Asph Paving Technol 2007;76:495–516.

[5] Huurman M, Mo LT, Woldekidan MF. Unravelling porous asphalt concrete: towards a mechanistic material design tool. Road Mater, Pavement Des 2009;10:233–62.

[6] Mo LT, Huurman M, Woldekidan MF, Wu SP, Molenaar AAA. Investigation into material optimization and development for improved ravelling resistant porous asphalt concrete. Mater Des 2010;31(7):3194–206.

[7] Flügge W. Viscoelasticity. Berlin, Heidelberg, New York: Springer-Verlag; 1975.

[8] Gemant A. A method of analyzing experimental results obtained from elasto-viscous bodies. Physics 1936;7:311–7.

[9] Bagley RL, Torvik PJ. A theoretical basis for the application of fractional calculus to viscoelasticity. J Rheol 1983;27(3):201–10.

[10] Huet C. Etude par une méthode d'impédance du comportement visco-élastique des matériaux hydrocarbonés. Paris: Faculté des Sciences de Paris; 1963.

[11] Pronk AC. The Huet–Sayegh model: a simple and excellent rheological model for master curves of asphaltic mixes. Baton Rouge, Louisiana, USA: ASCE; 2005.

[12] Benedetto HD, Mondher N, Sauzèat C, Olard F. Three-dimensional thermo-viscoplastic behaviour of bituminous materials. The DBN model. Road Mater, Pavement Des 2007;8(2):285–315.

[13] Pellinen T, Oeser M. Creep and recovery of linear and nonlinear rheological bodies. In: Proceedings of the international conference on advance characterization of pavement and soil engineering materials; 2007.
[14] Di Paola M, Pirrotta A, Valenza A. Visco-elastic behavior through fractional calculus: an easier method for best fitting experimental results. Mech Mater 2011;43(12):799–806.
[15] Schwartz CW, Gibson NH, Schapery R, Witczak MW. Viscoplasticity modeling of asphalt concrete behavior. 15th engineering mechanics division conference. Geotechnical Special Publication; 2003.
[16] Underwood SB, Kim RY. Viscoelastoplastic continuum damage model for asphalt concrete in tension. J Eng Mech 2011;137(11):732–9.
[17] Ha K, Schapery RA. A three-dimensional viscoelastic constitutive model for particulate composites with growing damage and its experimental verification. Int J Solids Struct 1998;35(26–27):3497–517.
[18] Giunta M, Pisano AA. One-dimensional visco-elastoplastic constitutive model for asphalt concrete. Multidiscip Model Mater Struct 2006;2(2):247–64.
[19] Darabi MK, Abu Al-Rub RK, Masad EA, Huang CW, Little DN. A thermo-viscoelastic–viscoplastic–viscodamage constitutive model for asphaltic materials. Int J Solids Struct 2011;48(1):191–207.
[20] Schapery R. On the characterization of nonlinear viscoelastic materials. Polym Eng Sci 1969;9(4):295–310.
[21] Perzyna P. Thermodynamic theory of viscoplasticity. Adv Appl Mech 1971;11:313–54.
[22] Masad E, Dessouky S, Little D. Development of an elastoviscoplastic microstructural-based continuum model to predict permanent deformation in hot mix asphalt. Int J Geomech 2007;7(2):119–30.
[23] Kachanov L. Time of the rupture process under creep conditions (in Russian). Isv Akad Nauk SSR Otd Tekh Nauk 1958;8:26–31.
[24] You T, Abu Al-Rub RK, Darabi MK, Masad EA, Little DN. Three-dimensional microstructural modeling of asphalt concrete using a unified viscoelastic–viscoplastic–viscodamage model. Constr Build Mater 2012;28:531–48.
[25] Pasetto M, Baldo N. Computational analysis of the creep behaviour of bituminous mixtures. Constr Build Mater 2015;94:784–90.
[26] de Espindola JJ, da Silva Neto JM, Lopes EMO. A generalised fractional derivative approach to viscoelastic material properties measurement. Appl Math Comput 2005;164:493–506.
[27] Wu Q, Wang C, Liang R, Liu Y, Cheng J, Kang Y. Fractional linear viscoelastic constitutive relations of anhydride-cured thermosetting rubber-like epoxy asphalt binders. Constr Build Mater 2018;170:582–90.
[28] Lagos-Varas M, Raposeiras AC, Movilla-Quesada D, Arenas JP, Castro-Fresno D, Muñoz-Cáceres O, et al. Study of the permanent deformation of binders and asphalt mixtures using rheological models of fractional viscoelasticity. Constr Build Mater 2020;260:120438.
[29] Wang LY, Zhou FX. Analysis of elastic-viscoplastic creep model based on variable-order differential operator. Appl Math Model 2020;81:37–49.
[30] Woldekidan MF, Huurman M, Pronk AC. A modified HS model: numerical applications in modeling the response of bituminous materials. Finite Elem Anal Des 2012;53:37–47.
[31] Kose S, Guler M, Bahia H, Masad E. Distribution of strains within asphalt binders in HMA using image and finite element techniques. Transp Res Rec 2000;1728:21–7.
[32] Abbas A, Masad E, Papagiannakis T, Harman T. Micromechanical modeling of the viscoelastic behavior of asphalt mixtures using the discrete-element method. Int J Geomech 2007;7(2):131–9.
[33] Dai Q, You Z. Micro-mechanical finite element framework for predicting visco-elastic properties of asphaltic mixtures. J Mater Struct 2008;41(6):1025–37.
[34] Huang Y, Yang Z, Ren W, Liu G, Zhang C. 3D meso-scale fracture modelling and validation of concrete based on in-situ X-ray computed tomography images using damage plasticity model. Int J Solids Struct 2015;67:340–52.
[35] Skarżyński Ł, Tejchman J. Experimental investigations of fracture process in concrete by means of X-ray micro-computed tomography. Strain 2016;52:26–45.
[36] Mazzucco G, Xotta G, Pomaro B, Salomoni VA, Faleschini F. Elastoplastic-damaged meso-scale modelling of concrete with recycled aggregates. Composites, Part B, Eng 2018;140:145–56.
[37] Mazzucco G, Pomaro B, Xotta G, Majorana CE, Salomoni VA. Tomography reconstruction of concrete materials for mesoscale modelling. Eng Comput 2020;37(7):2275–91.
[38] He H, Zheng J, Schaefer VR. Simulating shearing behavior of realistic granular soils using physics engine. Granul Matter 2021;23:56.
[39] Thilakarathna PSM, Kristombu Baduge S, Mendis P, Chandrathilaka ERK, Vimonsatit V, Lee H. Aggregate geometry generation method using a structured light 3D scanner, spherical harmonics-based geometry reconstruction, and placing algorithms for mesoscale modeling of concrete. J Mater Civ Eng 2021;33:04021198.
[40] Benkemoun N, Hautefeuille M, Colliat JB, Ibrahimbegovic A. Failure of heterogeneous materials: 3D meso-scale FE models with embedded discontinuities. Int J Numer Methods Eng 2010;82:1671–88.
[41] Ma HF, Xu WX, Li YC. Random aggregate model for mesoscopic structures and mechanical analysis of fully-graded concrete. Comput Struct 2016;177:103–13.
[42] Wang X, Zhang M, Jivkov AP. Computational technology for analysis of 3D meso-structure effects on damage and failure of concrete. Int J Solids Struct 2016;80:310–33.
[43] Aliha MRM, Ziari H, Mojaradi B, Sarbijan MJ. Modes I and II stress intensity factors of semi-circular bend specimen computed for two-phase aggregate/mastic asphalt mixtures. Theor Appl Fract Mech 2020;106:102437.
[44] Fadil H, Jelagin D, Partl MN. Spherical indentation test for quasi-non-destructive characterisation of asphalt concrete. Mater Struct 2022;55:102.
[45] Wang H, Wang J, Chen J. Micromechanical analysis of asphalt mixture fracture with adhesive and cohesive failure. Eng Fract Mech 2014;132:104–19.
[46] Han D, Liu G, Xi Y, Zhao Y, Tang D. Performance prediction of asphalt mixture based on dynamic reconstruction of heterogeneous microstructure. Powder Technol 2021;392:356–66.
[47] Wu ZY, Zhang JH, Yu HF, Ma HY. 3D mesoscopic investigation of the specimen aspect-ratio effect on the compressive behavior of coral aggregate concrete. Composites, Part B, Eng 2020;198:108025.
[48] Bai F, Li Y, Liu L, Li X, Liu W. An efficient and high-volume fraction 3D mesoscale modeling framework for concrete and cementitious composite materials. Compos Struct 2023;325:117576.
[49] Wei X, Sun Y, Gong H, Li Y, Chen J. Repartitioning-based aggregate generation method for fast modeling 3D mesostructure of asphalt concrete. Comput Struct 2023;281:107010.
[50] Mazzucco G, Pomaro B, Salomoni VA, Majorana CE. Numerical modelling of ellipsoidal inclusions. Constr Build Mater 2018;167:317–24.
[51] Majewski M, Holobut P, Kursa M, Kowalczyk-Gajewska K. Packing and size effects in elastic-plastic particulate composites: micromechanical modelling and numerical verification. Int J Eng Sci 2020;151:103271.
[52] Tan Z, Guo F-Q, Leng Z, Yang ZJ, Cao P. A novel strategy for generating mesoscale asphalt concrete model with controllable aggregate morphology and packing structure. Comput Struct 2024;296:107315.
[53] Wu X, Gao L, Du S. Mix proportion design of asphalt concrete. IOP Conf Ser, Mater Sci Eng 2017;275(1):012019. IOP Publishing.
[54] Cignoni P, Callieri M, Corsini M, Dellepiane M, Ganovelli F, Ranzuglia G. Meshlab: an open-source mesh processing tool. In: Eurographics Italian Chapter Conference; 2008. p. 129–36.
[55] https://meshmixer.com/ (last accessed May 2023).
[56] Ross B. Fractional calculus and its applications. Berlin-Heidelberg, Germany: Springer-Verlag; 1975.
[57] Podlubny I. Fractional differential equations: an introduction to fractional derivatives, fractional differential equations, to methods of their solution and some of their applications. San Diego: Academic Press; 1999.
[58] Sabatier J, Agrawal OP, Teneiro Machado JA, editors. Advances in fractional calculus: theoretical developments and applications in physics and engineering. Springer; 2007.
[59] Mainardi F. Fractional calculus and waves in linear viscoelasticity. Imperial College Press; 2010.
[60] Hopman PC, Nilsson RN, Pronk AC. Theory, validation and application of the viscoelastic multilayer program VEROAD. In: Proceedings of the eight international conference on asphalt pavements; 1997.
[61] Oldham KB, Spanier J. The fractional calculus: theory and applications of differentiation and integration to arbitrary order. Mathematics in Science and Engineering. London: Academic Press; 1974.
[62] Spanos PD, Evangelatos GI. Response of a non-linear system with restoring forces governed by fractional derivatives — time domain simulation and statistical linearization solution. Soil Dyn Earthq Eng 2010;30:811–21.
[63] Zhang W, Drescher A, Newcomb DE. Viscoelastic analysis of diametral compression of asphalt concrete. J Eng Mech 1997;123(6):596–603.
[64] Simo JC, Hughes TJ. Computational inelasticity, vol. 7. Springer Science & Business Media; 2006.
[65] de Souza Neto EA, Peric D, Owen DR. Computational methods for plasticity: theory and applications. John Wiley & Sons; 2011.
[66] Ossa EA, Deshpande VS, Cebon D. Phenomenological model for monotonic and cyclic behavior of pure bitumen. J Mater Civ Eng 2005;17(2):188–97.
[67] Bai F, Yang X, Zeng G. Creep and recovery behavior characterization of asphalt mixture in compression. Constr Build Mater 2014;54:504–11.
[68] Deshpande VS, Cebon D. Uniaxial experiments on idealized asphalt mixes. J Mater Civ Eng 2000;12(3):262–71.
[69] Mahyuddin A, Tjaronge MW, Ali N, Isran Ramli M. Experimental analysis on stability and indirect tensile strength in asphalt emulsion mixture containing buton granular asphalt. Int J Appl Eng Res 2017;12(12):3162–9.
[70] Weissmann S, Harvey JT, Sackman JL, Long F. Selection of laboratory test specimen dimension for permanent deformation of asphalt concrete pavements. In: Transportation research record, vol. 1681. 1997. Washington D.C.
[71] Zhou FP, Lydon FD, Barr BIG. Effect of coarse aggregate on elastic modulus and compressive strength of high performance concrete. Cem Concr Res 1995;25(1):177–86.
[72] Delaplace A, Toussaint F. Discrete element modeling of high performance concretes: effect of aggregates properties. In: Pijaudier-Cabot G, Grassl P, La Borderie C, editors. 10th international conference on fracture mechanics of concrete and concrete structures FraMCoS-X; 2019. p. 235355.